

KMT-2018-BLG-0748Lb: Sub-Saturn Microlensing Planet Orbiting an Ultracool Host

Cheongho Han¹, In-Gu Shin², Youn Kil Jung², Doeon Kim¹, Jennifer C. Yee³
(Leading authors)

and

Michael D. Albrow⁴, Sun-Ju Chung^{2,5}, Andrew Gould^{6,7}, Kyu-Ha Hwang², Chung-Uk Lee², Yoon-Hyun Ryu²,
Yossi Shvartzvald⁸, Weicheng Zang⁹, Sang-Mok Cha^{2,10}, Dong-Jin Kim², Hyoun-Woo Kim², Seung-Lee Kim^{2,5},
Dong-Joo Lee², Yongseok Lee^{2,10}, Byeong-Gon Park^{2,5}, and Richard W. Pogge⁷
(The KMTNet Collaboration),

¹ Department of Physics, Chungbuk National University, Cheongju 28644, Republic of Korea

² Korea Astronomy and Space Science Institute, Daejeon 34055, Republic of Korea

³ Center for Astrophysics | Harvard & Smithsonian 60 Garden St., Cambridge, MA 02138, USA

⁴ University of Canterbury, Department of Physics and Astronomy, Private Bag 4800, Christchurch 8020, New Zealand

⁵ Korea University of Science and Technology, 217 Gajeong-ro, Yuseong-gu, Daejeon, 34113, Republic of Korea

⁶ Max Planck Institute for Astronomy, Königstuhl 17, D-69117 Heidelberg, Germany

⁷ Department of Astronomy, Ohio State University, 140 W. 18th Ave., Columbus, OH 43210, USA

⁸ Department of Particle Physics and Astrophysics, Weizmann Institute of Science, Rehovot 76100, Israel

⁹ Department of Astronomy and Tsinghua Centre for Astrophysics, Tsinghua University, Beijing 100084, China

¹⁰ School of Space Research, Kyung Hee University, Yongin, Kyeonggi 17104, Republic of Korea
e-mail: cheongho@astro.ph.chungbuk.ac.kr

Received ; accepted

ABSTRACT

Aims. We announce the discovery of a microlensing planetary system, in which a sub-Saturn planet is orbiting an ultracool dwarf host.

Methods. We detect the planetary system by analyzing the short-timescale ($t_E \sim 4.4$ days) lensing event KMT-2018-BLG-0748. The central part of the light curve exhibits asymmetry due to the negative deviations in the rising part and the positive deviations in the falling part.

Results. We find that the deviations are explained by a binary-lens model with a mass ratio between the lens components of $q \sim 2 \times 10^{-3}$. The short event timescale together with the small angular Einstein radius, $\theta_E \sim 0.11$ mas, indicate that the mass of the planet host is very small. The Bayesian analysis conducted under the assumption that the planet frequency is independent of the host mass indicates that the mass of the planet is $M_p = 0.18^{+0.29}_{-0.10} M_J$, and the mass of the host, $M_h = 0.087^{+0.138}_{-0.047} M_\odot$, is near the star/brown dwarf boundary, but the estimated host mass is sensitive to the assumption about the planet hosting probability. High-resolution follow-up observations would lead to revealing the nature of the planet host.

Key words. gravitational microlensing – planets and satellites: detection – brown dwarfs

1. Introduction

As of the time of writing this article, 107 microlensing planets in 100 planetary systems were found.¹ Although these microlensing planets comprise a minor fraction of all known planets, microlensing provides an important method to complement other major planet detection methods because of its capability of detecting planets that are difficult to be found by other methods. See the review paper of Gaudi (2012) for various advantages of the microlensing method. Especially, the microlensing method enables one to find planets orbiting ultracool dwarfs and brown dwarfs (BDs). The most important attribute of the microlensing method to have this capability is that planetary microlensing signals rely on the direct gravitational influence of planets and their hosts. As a result, it is not needed to measure the host flux for

the detection of a planet, and this enables the method to detect planets orbiting very faint hosts and even dark objects.

Detecting planets around ultracool dwarfs is important for various reasons. The first importance lies in the fact that ultracool dwarfs are very common in the Galaxy. According to the present-day mass function (Chabrier 2003), the number density of stars increases down to the lower stellar mass limit of $\sim 0.08 M_\odot$. In addition, the extension of the mass function into the BD regime indicates that BD number density is comparable to the stellar one. Therefore, constructing a planet sample including those around ultracool dwarfs is essential to fully census the demographics of planets in the Galaxy. Second, planets around ultracool dwarfs provide a test bed to check the planet formation scenario. Ultracool dwarfs are the lowest mass objects formed through the process of collapsing molecular clouds (Luhman 2012). The low mass of the central object results in

¹ The Extrasolar Planets Encyclopedia (<http://exoplanet.eu>)

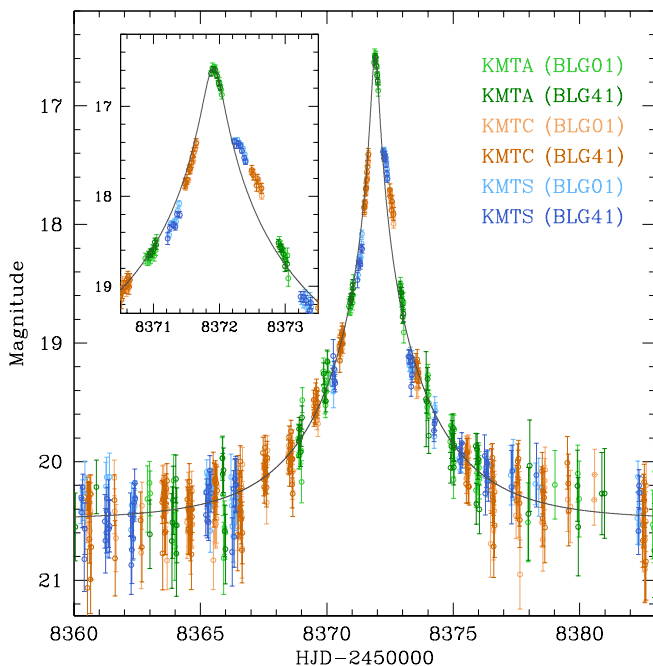


Fig. 1. Light curve of the lensing event KMT-2018-BLG-0748. The zoomed-in view around the peak is shown in the inset. The overplotted curve represents the 1L1S model.

the low mass of the accretion disk, and thus the environment of planet formation for ultracool dwarfs would be different from that of regular stars. With a sample of planets formed in different environment, it would be possible to probe the planet formation process in limiting conditions (Payne & Lodato 2007).

In this paper, we report a microlensing planetary system, in which a sub-Saturn planet orbits an ultracool dwarf. We present the analysis conducted for the planet discovery according to the following organization. In Section 2, we describe the observations of the lensing event from which the planet is detected. In Section 3, we describe various models tested for the interpretation of the data. In Section 4, we explain the procedure of determining the source type and the angular radius of the Einstein ring. In Section 5, we estimate the mass and distance to the lens. Discussions on the importance of the discovered planetary system and future follow-up observations to refine the physical lens parameters are given in Section 6. Summary of the results and conclusion are presented in Section 7.

2. Data

The lensing event from which the planetary system is discovered is KMT-2018-BLG-0748. The source (lensed star) of the event lies toward the bulge field at $(R.A., \text{decl.})_{J2000} = (17 : 51 : 29.88, -30 : 38 : 47.00)$, corresponding to $(l, b) = (-0^\circ.808, -1^\circ.974)$. The event reached its peak magnification of $A_{\text{peak}} \sim 30$ on 2018-09-10 ($\text{HJD}' \equiv \text{HJD} - 2450000 \sim 8372$). The event duration, defined by the time span of the source brightening beyond the photometric scatter, is about 6 days.

The event was found by the Korea Microlensing Telescope Network (KMTNet; Kim et al. 2016) survey. The survey commenced its alert-finder system in 2018 (Kim et al. 2018b), but only for a subset of its fields that did not include those containing KMT-2018-BLG-0748. Hence, the event was found from the post-season investigation of the data conducted by Kim et al.

(2018a). The event was in the field covered by another lensing survey of the Optical Gravitational Microlensing Experiment (OGLE; Udalski et al. 2015), but no trace of lensing signal was detected because of the source location at the edge of a camera chip.

Although the event lasted a short period of time, the light curve was continuously and densely covered. This coverage was possible thanks to two main reasons. First, the event was observed using multiple telescopes that were globally distributed in three continents. The individual KMTNet telescopes are located at the Siding Springs Observatory (KMTA) in Australia, the Cerro Tololo Inter-American Observatory (KMTC) in South America, and the South African Astronomical Observatory (KMTS) in Africa. The three telescopes are identical with a 1.6 m aperture. The $9\text{k} \times 9\text{k}$ mosaic camera mounted on each telescope yields a very wide field of view of 4 deg^2 , and this enables high-cadence observations of the event. Second, the source is positioned in the overlapping region of the two fields, for which the observational cadence was highest among the total 27 KMTNet fields. The two fields, BLG01 and BLG41, were laid out to overlap each other in most covered area, with a small offset between the fields to cover the gaps among the camera chips. The individual fields were monitored with a 30 min cadence, resulting in a combined cadence of 15 min. Observations were primarily carried out with the *I* band, and a subset of *V*-band images were acquired to measure the color of the source star.

Photometry of data are conducted using the KMTNet pipeline (Albrow et al. 2009), that utilizes the difference imaging method developed by Tomaney & Crofts (1996) and Alard & Lupton (1998). For a subset of the data, we conduct an extra photometry with the pyDIA code (Albrow 2017) to estimate the color of the source star. In Section 4, we describe the detailed procedure of estimating the source color. We rescale the error bars of the data estimated from the photometry pipeline using the method of Yee et al. (2012).

3. Interpretation of light curve

3.1. Single-lens (1L1S) model

The lensing light curve of KMT-2018-BLG-0748 is shown in Figure 1. At a casual glance, the light curve seems to be that of a standard event involved with a single lens and a single source (“1L1S”), and thus we first model the light curve under the 1L1S interpretation. Three parameters characterize a 1L1S lensing light curve. These parameters are t_0 , u_0 , and t_E , which represent the time of the minimum lens-source (projected) separation, the separation between the lens and source (scaled to the angular Einstein radius θ_E) at t_0 (impact parameter), and the event timescale, respectively.

The 1L1S model curve is plotted over the data points in Figure 1. The modeling is conducted so that the peak of the model matches the observed peak at $t_0 \sim 8371.9$. From the comparison of the observed data with the model, it appears that the observed light curve is approximately described by a 1L1S model with an event timescale of $t_E \sim 4$ days. However, a close inspection reveals that there exist slight deviations from the model, especially in the region around the peak. See the inset showing the enlarged view of the light curve around the peak.

In order to inspect the detailed structure of the deviations, we display the peak region of the light curve in Figure 2. We also show the residuals from the 1L1S model in the bottom panel. From the inspection of the residuals, it is found that the deviations occur in two major parts. The first part is the re-

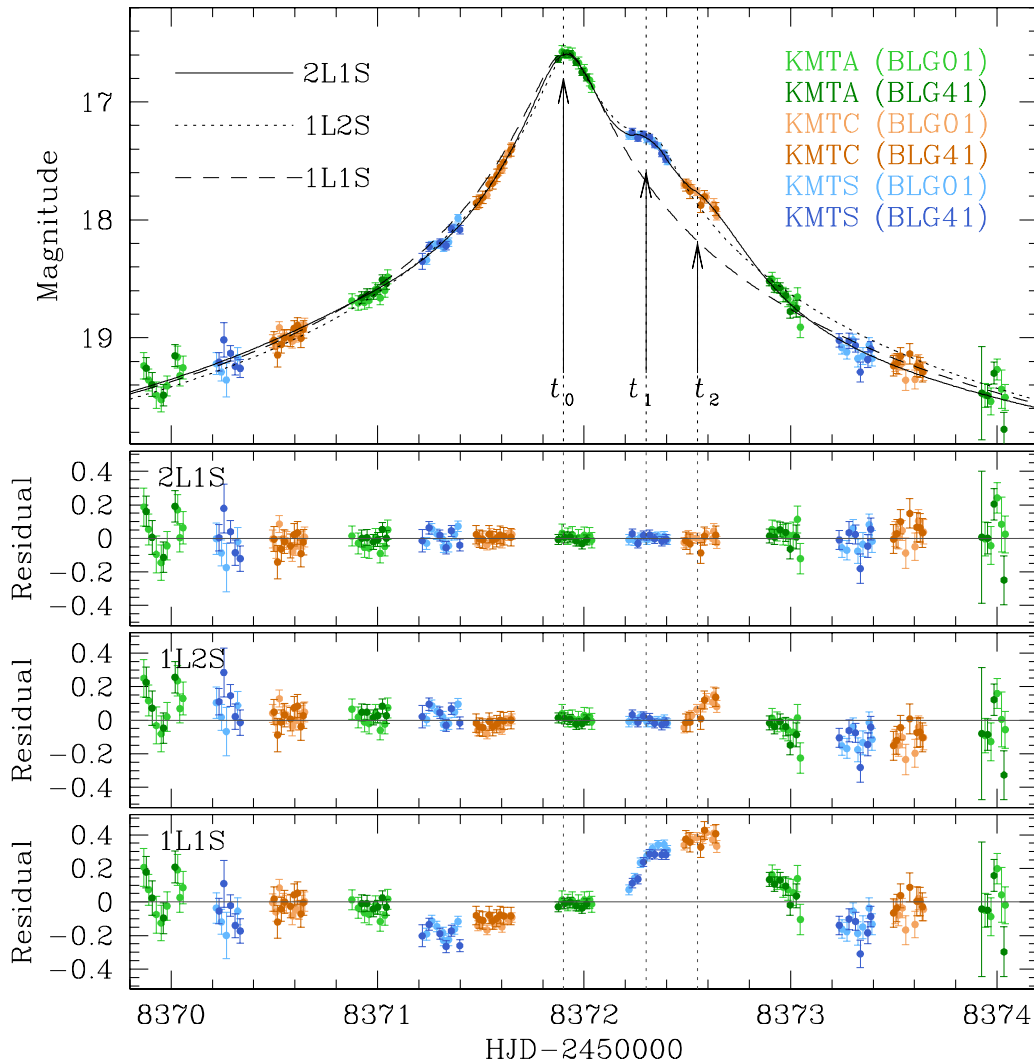


Fig. 2. Various tested models and their residuals. The top panel shows the three tested models, 2L1S (solid curve), 1L2S (dotted curve), and 1L1S (dashed curve) models, and the three lower panels show the residuals from the individual models. The three times marked at $t_0 \sim 8371.9$, $t_1 \sim 8372.3$, and $t_2 \sim 8372.6$ represent the peak time, and the two bumps, respectively.

gion in the rising side of the light curve before the peak during $8371.2 \lesssim \text{HJD}' \lesssim 8371.7$. The data points in this region exhibit negative deviations with respect to the 1L1S model. The second part is the region in the falling side after the peak during $8372.2 \lesssim \text{HJD}' \lesssim 8373.0$. In contrast to the first part, the data points in this region exhibit positive deviations. To be noted is that the deviations in this region exhibit two bumps at $t_1 \sim 8372.3$ and $t_2 \sim 8372.6$, and the positive deviations are followed by slight negative deviations during $8373.2 \lesssim \text{HJD}' \lesssim 8373.5$. The combination of the negative deviations in the rising side and the positive deviations in the falling side makes the light curve appear to be asymmetric.

A lensing light curve may become asymmetric due to two major reasons. The first is the binarity of the lens and the other is the binarity of the source. Acceleration of the observer induced by the orbital motion of the Earth can also cause a light curve to appear asymmetric, but for short-timescale events like KMT-2018-BLG-0748, these microlens-parallax effects (Gould et al. 1994) cannot be the cause of the light curve asymmetry because the deviation of the source motion from rectilinear during the short duration of the lensing magnification is negligible.

Table 1. Lesing parameters of 1L2S model

Parameter	Value
χ^2	1145.8
$t_{0,1}$ (HJD')	8371.918 ± 0.004
$t_{0,2}$ (HJD')	8372.336 ± 0.006
$u_{0,1}$	0.052 ± 0.002
$u_{0,2}$	0.033 ± 0.002
t_E (day)	3.54 ± 0.11
q_F	0.20 ± 0.02

Notes. $\text{HJD}' = \text{HJD} - 2450000$.

3.2. Binary-source (1L2S) model

To investigate the cause of the deviations from the 1L1S model, we first test a model in which the source is composed of two stars (“1L2S” model). Adding one more source component to the lens modeling requires one to include additional parameters together with the 1L1S parameters, i.e., (t_0, u_0, t_E) . Following the parameterization of Hwang et al. (2013), these parameters are $t_{0,2}$, $u_{0,2}$, and q_F , representing the peak time and impact parameters of the

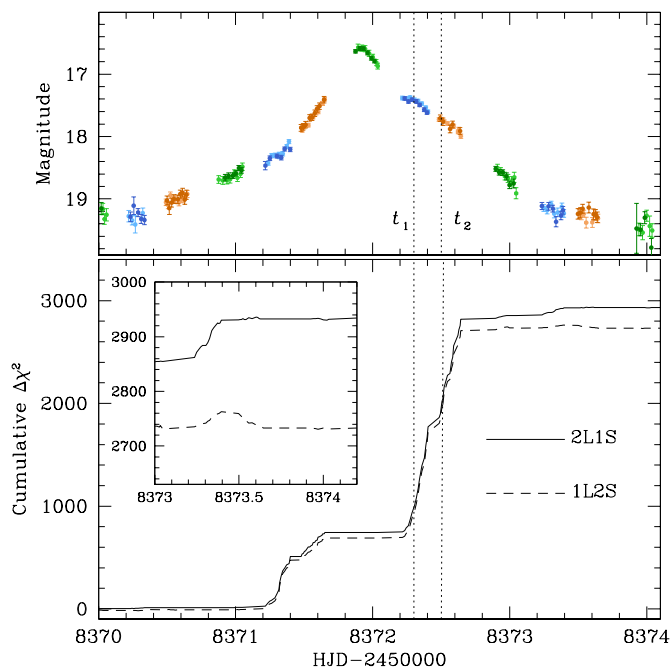


Fig. 3. Cumulative $\Delta\chi^2$ distributions of the 2L1S (solid curve) and 1L2S (dashed curve) models with respect to the 1L1S model. The observed light curve is shown in the upper panel to see the locations around which the fit improves. The zoomed-in view of the 2L1S and 1L2S distributions in the region of $8373.0 \leq \text{HJD}' \leq 8374.2$ is shown in the inset of the lower panel. The times marked by t_1 and t_2 corresponds to the times of the two bumps marked in Fig. 2.

second source, and the flux ratio of the second source to the first source, respectively. To designate the peak time and impact parameter associated with the primary source, we use the notations $t_{0,1}$ and $u_{0,1}$, respectively. Modeling is done using the initial parameters estimated from the 1L1S modeling and considering the deviation features.

The lensing parameters of the 1L2S model, together with the χ^2 value of the fit, are listed in Table 1. The model curve (dotted curve in the top panel) and residuals (presented in the third panel labeled as “1L2S”) from the model are shown in Figure 2. Comparison of the model fits indicates that the 1L2S model provides a substantially better fit than the 1L1S model by $\Delta\chi^2 = 2739.6$. To inspect how the introduction of a source companion improves the fit, we construct the cumulative distribution of $\Delta\chi^2$ between the 1L2S and 1L1S models and present the distribution in Figure 3. According to the 1L2S model, the second source, which is fainter than the first source by $\Delta I = -2.5 \log q_F \sim 1.75$ magnitude, trails the primary source with a time gap of $\Delta t = t_{0,2} - t_{0,1} \sim 0.42$ days (~ 10 hours) and approaches the lens with a smaller impact parameter ($u_{0,2} \sim 0.033$) than that of the primary source ($u_{0,1} \sim 0.052$). We consider finite-source effects to investigate whether the lens passes over the surfaces of the source stars, but it is found that the impact parameters of both source trajectories are greater than the source radii, and thus there is no trace of finite-source effects. The introduction of a binary source substantially reduces the negative residuals in the rising side of the light curve. The 1L2S model also reduces the positive residuals in the the falling side. However, the model leaves noticeable deviations around the bump at t_2 and in the negative deviation region during $8373.0 \leq \text{HJD}' \leq 8373.5$.

The validity of the 1L2S model can be additionally checked with the use of the V -band data, because the V -band data points

Table 2. Lensing parameters of 2L1S model

Parameter	Value
χ^2	937.6
t_0 (HJD')	8371.901 ± 0.004
u_0	0.034 ± 0.002
t_E (day)	4.38 ± 0.15
s	0.939 ± 0.003
q (10^{-3})	2.03 ± 0.15
α (rad)	-0.023 ± 0.008
ρ (10^{-3})	10.89 ± 0.97

Notes. HJD' = HJD – 2450000.

near the maximum magnification of the second source would manifest a color change (Gaudi 1998; Hwang et al. 2013). Unfortunately, this test cannot be done because the peak region of the second source magnification is sparsely covered by the V -band data, and the photometry quality of the few data points is not good enough to securely measure the color change induced by the binary source.

3.3. Binary-lens (2L1S) model

We also test a model in which the lens is a binary (“2L1S” model). Similar to the 1L2S modeling, considering one more lens component requires one to add extra parameters to the lens modeling. These parameters are the s , q , and α , and they denote the projected separation between the lens components M_1 and M_2 , the mass ratio, i.e., $q = M_2/M_1$, and the source trajectory angle measured from the M_1 – M_2 axis, respectively. A binary lens induces caustics, at which a point-source lensing magnification becomes infinite, and the lensing light curve of a caustic-crossing event deviates from that of a point-source event due to the effect of a finite source size. We consider this finite-source effect in modeling by adding one more parameter of ρ , which is defined as $\rho = \theta_*/\theta_E$ (normalized source radius). Here θ_* denotes the angular size of the source radius. Finite-source magnifications are computed using the numerical method based on the ray-shooting algorithm (Dong et al. 2006). In this process, we take account of the surface brightness variation of the source caused by limb darkening. We assume that the surface brightness linearly decreases and choose the limb-darkening coefficients considering the spectral type of the source. We discuss the detailed procedure of the source type determination in Section 4. With the surface-brightness model $S \propto 1 - \Gamma(1 - 1.5 \cos \psi)$, we adopt $(\Gamma_V, \Gamma_I) = (0.62, 0.49)$ for the coefficients in V and I bands, respectively. Here ψ represents the angle between two vectors, with origin at the source center and pointing toward the observer and to the source surface.

In the 2L1S modeling, the lensing parameters are categorized into two groups. The parameters (s, q) in the first group are searched for using a grid approach because a lensing magnification can change dramatically with a minor variation of the parameters. For the other parameters, i.e., $(t_0, u_0, t_E, \alpha, \rho)$, in contrast, the magnification variation is smooth, and thus we look for these parameters using a downhill method based on the Markov Chain Monte Carlo (MCMC) algorithm. The grid search for the parameters (s, q) is useful because investigating the $\Delta\chi^2$ map on the plane of these parameters enables one to find possible degenerate solutions, which yield similar models despite the large differences in the lensing parameters. For KMT-2018-BLG-0748, we identify a unique solution without any degeneracy. With the

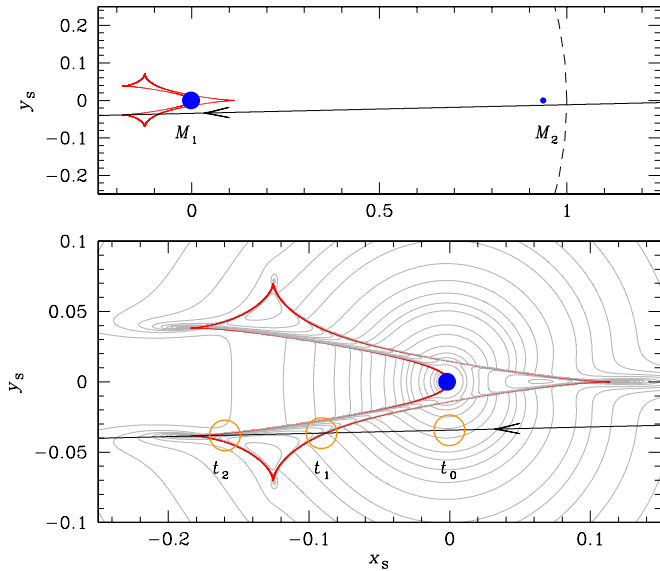


Fig. 4. Configuration of the lens system for the 2L1S solution. The upper panel shows the zoomed-out region encompassing the binary lens components, blue dots marked by M_1 and M_2 , and the lower panel shows the zoomed-in view of the central magnification region. The line with an arrow indicates the source trajectory, the cuspy closed curve is the caustic, and the dashed circle in the upper panel represents the Einstein ring. In the lower panel, the three empty circles on the trajectory of the source indicate the source locations corresponding to the times of t_0 , t_1 , and t_2 marked in Fig. 2. The circle size is scaled to θ_E . The grey curves in the lower panel represent equi-magnification contours.

rough position of the local in the s - q plane, we then conduct another modeling to find a refined solution by setting, in this time, all lensing parameter, including s and q , as free parameters.

The model curve (solid curve in the top panel) obtained from the 2L1S modeling and the residuals (second panel labeled as “2L1S”) from the model are shown in Figure 2. The lensing parameters of the model are presented in Table 2 together with the χ^2 value of the fit. To be noted among the parameters is that the estimated value of $q \sim 2 \times 10^{-3}$ is very low, suggesting that the companion to the lens is very likely to be a planet.

We find that the 2L1S model well explains the observed light curve. The relative goodness of the 2L1S model over the other models is shown in the cumulative $\Delta\chi^2$ distribution presented in Figure 3. The 2L1S model improves the fit by $\Delta\chi^2 = 2947.0$ with respect to the 1L1S model. The model fit is better than that of the 1L2S model by $\Delta\chi^2 = 208.2$, and the residuals from the 1L2S models, i.e., the bump at around t_2 and the negative deviations during $8373.0 \lesssim \text{HJD}' \lesssim 8373.5$, vanish. This indicates that the observed deviations are explained by a lens companion rather than a source companion.

The configuration of the lens system according to the 2L1S solution is provided in Figure 4. In the figure, locations of the binary lens components are marked by blue dots, the source trajectory is represented by a line with an arrow, and the caustic is shown in red color (cuspy closed curve). We note that the separation between M_1 and M_2 , $s \sim 0.94$, is similar to θ_E , and this results in a single resonant caustic. The caustic has two prongs extending from the position of the primary lens. The source moves along the path that is nearly parallel to the M_1 - M_2 axis, approaching the primary lens, and crossing the lower prong of the caustic two times, i.e., caustic entry and exit. The time of the source approach to the primary lens corresponds to the time of

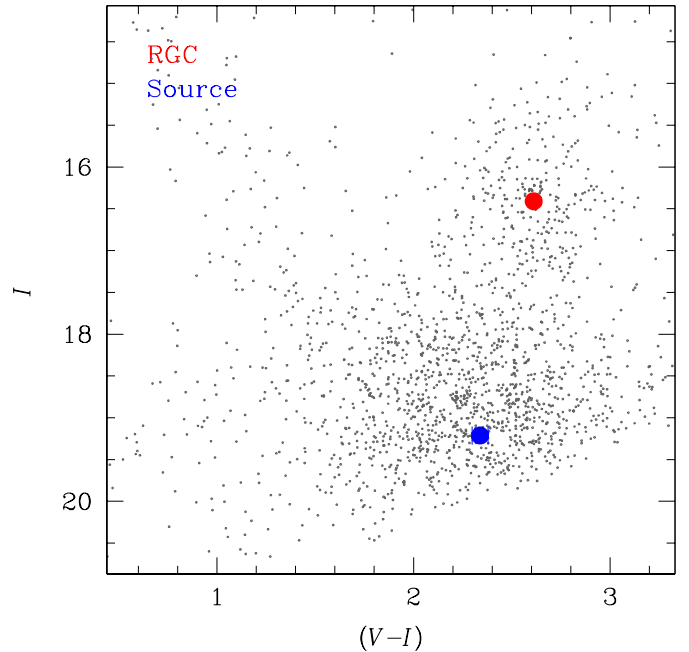


Fig. 5. Color-magnitude diagram of stars located within $2' \times 2'$ region around the source. The blue and red dots represent the positions of the source and RGC centroid, respectively.

the peak magnification, t_0 , and the times of the caustic crossings correspond to the times of the bumps in the light curve at t_1 and t_2 marked by arrows in Figure 2. A caustic crossing, in general, results in a rapid rising of the lensing magnification, yielding a spike feature in lensing light curves. For KMT-2018-BLG-0748, however, finite-source effects are severe, and thus the caustic crossings result in minor bumps instead of spike features. According to the 2L1S model, the slight negative deviations from the 1L1S model during $8372.2 \lesssim \text{HJD}' \lesssim 8373.0$ are explained by the excess magnification extending from the tip of the caustic. We note that these negative deviations and the bump at t_2 cannot be explained by the 1L2S model.

Table 3. Estimated values of θ_* , θ_E and μ

Parameter	Value
θ_* (μas)	1.21 ± 0.10
θ_E (mas)	0.111 ± 0.010
μ (mas yr $^{-1}$)	9.24 ± 0.80

4. Angular Einstein radius

We estimate θ_E from the measured value of ρ by $\theta_E = \theta_*/\rho$. For this, we first estimate θ_* based on the de-reddened color, $(V-I)_0$, and brightness, I_0 , of the source using the method of Yoo et al. (2004). According to the procedure of this method, we locate the source in the instrumental color-magnitude diagram (CMD), measure the offsets of the source in color, $\Delta(V-I)$, and brightness, ΔI , from the centroid of the red giant clump (RGC), and then estimate $(V-I)_0$ and I_0 using the relation

$$(V-I, I)_0 = (V-I, I)_{\text{RGC},0} + \Delta(V-I, I). \quad (1)$$

Here $(V-I, I)_{\text{RGC},0} = (1.06, 14.47)$ denote the known values of the RGC centroid from Bensby et al. (2013) and Nataf et al. (2013), respectively.

Figure 5 shows the source and RGC centroid in the CMD of stars in the vicinity of the source. We note that the CMD is produced by conducting photometry on the KMTC data set using the pyDIA software, but the color and brightness are scaled to those of the OGLE-III system (Szymański et al. 2011) to present the calibrated color and brightness. The measured positions of the source and RGC centroid are $(V-I, I) = (2.34 \pm 0.04, 19.21 \pm 0.03)$ and $(V-I, I)_{\text{RGC}} = (2.61, 16.41)$, respectively. By measuring the offsets of $\Delta(V-I, I) = (-0.27, 2.80)$, we estimate that the source has a de-reddened color and a brightness of

$$(V-I, I)_0 = (0.79 \pm 0.04, 17.27 \pm 0.03). \quad (2)$$

From the measured color and brightness, it is found that the source is a turn-off star with a spectral type of late G.

The angular radius of the source is deduced from its color and brightness. For this, we first estimate $V-K$ from the measured $V-I$ using the relation between the two colors (Bessell & Brett 1988), and then estimate θ_* using the relation between $(V-K)$ and θ_* (Kervella et al. 2004). This process yields the source radius of

$$\theta_* = 1.21 \pm 0.10 \mu\text{as}. \quad (3)$$

With the estimated θ_* , the Einstein radius and the relative lens-source proper motion are estimated by

$$\theta_E = \frac{\theta_*}{\rho} = 0.111 \pm 0.013 \text{ mas}, \quad (4)$$

and

$$\mu = \frac{\theta_E}{t_E} = 9.24 \pm 1.11 \text{ mas yr}^{-1}, \quad (5)$$

respectively. The values of θ_* , θ_E , and μ are summarized in Table 3. Considering that typical lensing events, generated by M dwarfs located roughly halfway between the observer and source, results in $\theta_E \sim 0.5$ mas, the measured θ_E value is significantly smaller than those of typical events. Because $\theta_E \propto M^{1/2}$, the small value of θ_E suggests that the lens is a low-mass object. In contrast, the measured relative proper motion, ~ 9.2 mas yr $^{-1}$, is considerably higher than a typical value of ~ 5 mas yr $^{-1}$.

5. Physical lens parameters

The physical lens parameter of the mass, M , and distance, D_L , are unambiguously determined by measuring the two observables of θ_E and π_E , i.e.,

$$M = \frac{\theta_E}{\kappa\pi_E}; \quad (6)$$

and

$$D_L = \frac{\text{au}}{\pi_E\theta_E + \pi_S}. \quad (7)$$

Here π_E is the microlens parallax, $\kappa = 4G/(c^2\text{au})$, and π_S denotes the parallax to the source (Gould 2000b). Among the two observables needed to determine M and D_L , θ_E is measured, but π_E is not measured in the case of KMT-2018-BLG-0748, and this makes it difficult to determine the physical parameters using the relations in Equations (6) and (7). We, therefore, estimate M and D_L from a Bayesian analysis using the priors for the Galactic model and lens mass function together with the measured values of t_E and θ_E .

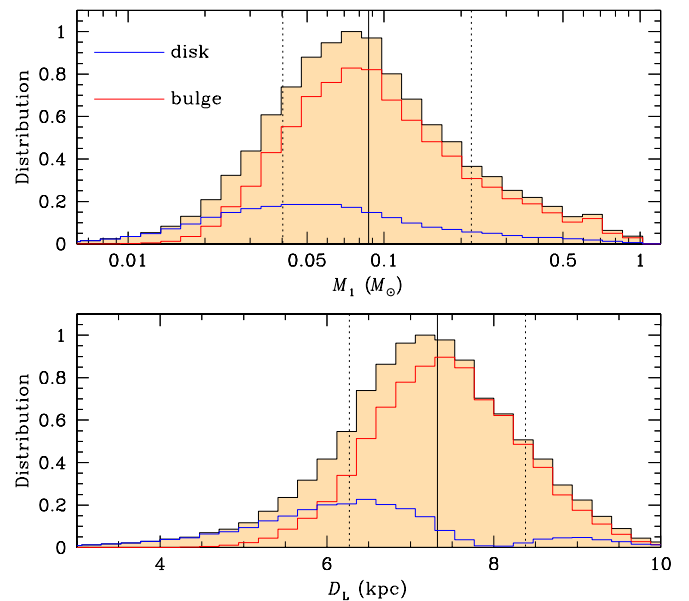


Fig. 6. Bayesian posteriors for the host mass (upper panel) and distance (lower panel) estimated from the Bayesian analysis. In each panel, the blue and red curves are the distributions contributed by disk and bulge lenses, respectively, and the black curve is that of the two lens populations combined. The solid and dotted vertical lines indicate the median and 1σ range, respectively.

The Bayesian analysis is conducted by generating numerous (4×10^7) artificial lensing events from a Monte Carlo simulation based on the prior models. In the simulation, lenses are physically distributed following a modified Han & Gould (2003) model and the lens-source transverse speeds of events are assigned based on the modified dynamical distributing model of Han & Gould (1995). Compared to the original Han & Gould (2003) model, in which the Galaxy disk is modeled by a simple double-exponential disk, the disk in the modified model has a form of

$$\rho_{\text{disk}} = \rho_{\text{disk},0} \left[e^{-(b^2+a^2/h_{R+}^2)^{1/2}} - e^{-(b^2+a^2/h_{R-}^2)^{1/2}} \right], \quad (8)$$

by adopting the disk model of Bennett et al. (2014). Here $\rho_{\text{disk},0} = 1.1 M_{\odot}/\text{pc}^3$ represents the matter density in the solar neighborhood, $a = [R^2 + (z/h_z)^2]^{1/2}$, $h_z = 79$ pc, $b = 0.5$, $(h_{R+}, h_{R-}) = (2530, 1320)$ pc, and (R, z) represent the position in the Galactocentric cylindrical coordinates. This modification is done to prevent the increase of the disk density all the way to the Galactic center. The dynamical model of disk objects is modified to account for the change in the matter distribution by changing the velocity dispersions along the (R, z) directions as $\sigma_R = \sigma_{R,0}[\Sigma(D_L)/\Sigma(D_L=0)]^{1/2}$ and $\sigma_z = \sigma_{z,0}[\Sigma(D_L)/\Sigma(D_L=0)]^{1/2}$, where $(\sigma_{R,0}, \sigma_{z,0}) = (30, 20)$ km s $^{-1}$ represent the velocity dispersions in the solar neighborhood along the (R, z) directions, respectively. For the bulge velocity dispersions, we use the mean values measured by *Gaia*. Considering the short timescale and small θ_E of KMT-2018-BLG-0748, lens masses are assigned using the mass function model of Zhang et al. (2019), which extends down to a substellar mass regime. In the mass function model, we consider remnant lenses, i.e., white dwarfs, neutron stars, and black holes, by adopting the Gould (2000a) model. We compute the posteriors for M and D_L by obtaining the probability distributions of events with values of t_E and θ_E located within the uncertainty ranges of the measured t_E and θ_E . We,

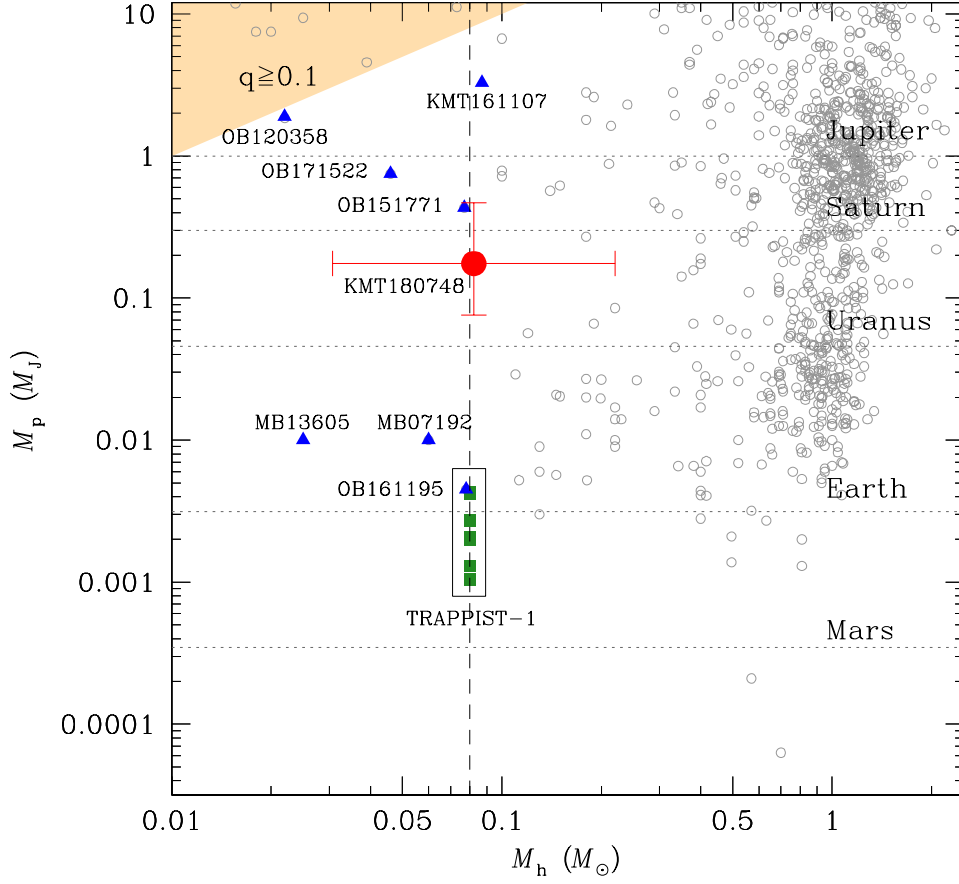


Fig. 7. Distribution of planets in the plane of the host, M_h , and planet, M_p , masses for planetary systems with known masses. Planetary systems with host masses at around or below the stellar mass limit are marked by colored points: a red dot for KMT-2018-BLG-0748L, blue triangle dots for the other microlensing planetary systems, and green square dots for the seven planets in TRAPPIST-1 system. The yellow shaded area represents the region with mass ratios $q = M_p/M_h \geq 0.1$. The dashed vertical line represents the star/BD boundary. The dotted horizontal lines represent the masses of the Jupiter, Saturn, Uranus, Earth, and Mars of the Solar system from the top to bottom.

then, use the median as a representative value and the 16% and 84% ranges of the distributions as the uncertainty range of the parameter.

Figure 6 shows the Bayesian posteriors for the primary lens mass M_1 (upper panel) and D_L (lower panel). In each panel, we present three distributions, in which the blue and red curves are the distributions contributed by disk and bulge lens populations, respectively, and the black curve is the sum of the two lens populations. We find that the disk and bulge contributions are 23% and 77%, respectively. The estimated masses of the primary and companion of the lens are

$$M_1 = 0.087^{+0.132}_{-0.047} M_\odot, \quad (9)$$

and

$$M_2 = 0.19^{+0.28}_{-0.10} M_J, \quad (10)$$

respectively. The planet mass is $\sim 0.63 M_S$ in units of Saturn's mass, and thus the planet is a sub-Saturn planet. We note that the mass of the primary approximately corresponds to the star/BD boundary. Considering that the uncertainty of the estimated mass is substantial, the exact nature of the planet host is unclear. The estimated distance to the lens is

$$D_L = 7.3^{+1.1}_{-1.1} \text{ kpc}. \quad (11)$$

Table 4. Physical lens parameters

Parameter	Value
$M_1 (M_\odot)$	$0.087^{+0.132}_{-0.047}$
$M_2 (M_J)$	$0.19^{+0.28}_{-0.10}$
D_L (kpc)	$7.3^{+1.1}_{-1.1}$
a_\perp (au)	$0.62^{+0.09}_{-0.09}$

The projected planet-host separation is

$$a_\perp = sD_L\theta_E = 0.62^{+0.09}_{-0.09} \text{ au}. \quad (12)$$

The planetary separation is much bigger than the snow line of $a_{sl} \sim 2.7 \text{ au}(M_1/M_\odot) \sim 0.23 \text{ au}$. The estimated physical lens parameters of M_1 , M_2 , D_L , and a_\perp are listed in Table 4.

We note that the estimates of the planet and host masses can vary depending on the assumption about the planet hosting probability. In our analysis, we assume that the planet frequency is independent of the host mass or the planet/host mass ratio. Laughlin et al. (2004) discussed the possibility of the planet frequency dependency on the host mass by pointing out that, within the core accretion paradigm, giant planets would be difficult to be formed around low-mass M dwarfs, while such planets would be common around solar-type stars. Vanderou et al. (2020) addressed this issue from a microlensing perspective by showing that the host mass of the planet MOA-2013-BLG-220Lb

(Yee et al. 2014), with a planet/host mass ratio of $q \sim 3 \times 10^{-3}$, determined by analyzing the constraint from high-resolution AO observations was substantially more massive than the value estimated from the Bayesian analysis conducted under the assumption that stars of all masses were equally likely to host planets of a given mass ratio. From this result, they suggested that planets with planet/host mass ratios $q \sim 2\text{--}3 \times 10^{-3}$ might be more likely to be hosted by higher mass hosts. Under this prediction, then, the mass of KMT-2018-BLG-0748L would be more massive than the mass presented in Equation (9).

6. Discussion

The planetary system KMT-2018-BLG-0748L illustrates that microlensing provides an important tool to detect planets orbiting very low-mass stellar and sub-stellar hosts. To demonstrate the importance of microlensing in detecting such planetary systems, in Figure 7, we present the distribution of planets in the plane of the host, M_h , and planet, M_p , masses for planetary systems with known masses. There exist nine planetary systems, including KMT-2018-BLG-0748L, with host masses at around or below the star/BD mass limit of $\sim 0.08 M_\odot$. These planetary systems include MOA-2007-BLG-192L (Bennett et al. 2008; Gould et al. 2010; Kubas et al. 2012), OGLE-2012-BLG-0358L (Han et al. 2013), MOA-2013-BLG-605L (Sumi et al. 2016), OGLE-2015-BLG-1771L (Zhang et al. 2019), OGLE-2016-BLG-1195L (Bond et al. 2017; Shvartzvald et al. 2017), KMT-2016-BLG-1107 (Hwang et al. 2019), OGLE-2017-BLG-1522L (Jung et al. 2018), and TRAPPIST-1 (Gillon et al. 2016, 2017).² We mark these planetary systems by colored points: a red dot for KMT-2018-BLG-0748L, blue triangle dots for the other microlensing planetary systems, and green square dots for the seven planets in TRAPPIST-1 system. Among these systems, eight were detected using the microlensing method except for TRAPPIST-1, which was discovered using the transit method.

We note that the exact nature of the planet host can be identified from future high-resolution follow-up observations. Considering that the mass of the planet host lies at around the star/BD boundary and the uncertainty of the estimated mass from the Bayesian analysis is large, it is not clear whether the host is a low-mass star or a BD. Revealing the nature of the host is possible if the lens is resolved from the source by conducting high-resolution follow-up observations. KMT-2018-BLG-0748 is an appropriate target for such observations because the relative proper motion, $\mu \sim 9.2 \text{ mas yr}^{-1}$, is substantially higher than typical lensing events. Bennett et al. (2007) suggested the possibility of detecting the lens and source with high-resolution space-based follow-up observations, and this was realized by the detection of the lens star for the planetary microlensing event OGLE-2005-BLG-169 from the *Hubble Space Telescope* observations conducted when the lens-source separation was $\sim 49 \text{ mas}$ (Bennett et al. 2015). The lens of the same event was also detected from the ground-based AO observations using the Keck telescope conducted by Batista et al. (2015). Observations by the *James Webb Space Telescope* (JWST) would be able to probe much lower masses than observations by existing AO systems, because the sensitivity of ground-based observations is limited by the bright sky background in the infrared. By implementing a criterion of $\sim 50 \text{ mas}$ separation for the lens and

source resolution, the lens of KMT-2018-BLG-0748 could be resolved ~ 5.4 years after the discovery of the event, i.e., in early 2024.

However, in the case of KMT-2018-BLG-0748, one should adopt a significantly more conservative approach to future AO observations so that a non-detection would be unambiguously interpreted as due to the host being a sub-stellar object. That is, first, one should conservatively estimate the proper motion as $\mu > 7 \text{ mas yr}^{-1}$. And second, one should make allowances for the possibility of a large flux ratio between the lens and source due to the ultracool nature of the first, and so require $\Delta\theta > 70 \text{ mas}$. Thus, to confidently exclude stellar-mass lenses in the event of a non-detection requires waiting $\Delta t = \Delta\theta/\mu > 10$ years, i.e., until 2028.

7. Conclusion

The lensing event KMT-2018-BLG-0748 was analyzed and the results from the analysis were presented. For the event, the central part of the light curve appeared to be asymmetric with respect to the 1L1S model due to the negative deviations in the rising side and the positive deviations in the falling side. We tested various models and found that the deviations were explained by a binary-lens model with a mass ratio between the components of $q \sim 2 \times 10^{-3}$. The small angular Einstein radius, $\theta_E \sim 0.11 \text{ mas}$, indicated that the mass of the planet host was very low. From the Bayesian analysis conducted under the assumption of no dependency of the planet frequency on the host mass, it was estimated that the planet had a mass $M_p = 0.18_{-0.10}^{+0.29} M_J$ and the mass of the host, $M_h = 0.087_{-0.047}^{+0.138} M_\odot$, was at around the star/BD boundary, but the host mass would vary depending on the assumption about the planet host probability. Resolving the lens and source would be possible in 2028, provided that the lens is luminous. In that case, the lens mass will be determined from these observations. If the measurement fails to detect the lens, this will imply that the lens is non-luminous and therefore, almost certainly, sub-stellar. In either case, these observations would resolve the nature of the planet host.

Acknowledgements. Work by CH was supported by the grants of National Research Foundation of Korea (2017R1A4A1015178 and 2019R1A2C2085965). Work by AG was supported by JPL grant 1500811. This research has made use of the KMTNet system operated by the Korea Astronomy and Space Science Institute (KASI) and the data were obtained at three host sites of CTIO in Chile, SAAO in South Africa, and SSO in Australia.

References

- Alard, C., & Lupton, R. H. 1998, *ApJ*, 503, 325
- Albrow, M. 2017, MichaelDAlbrow/pyDIA: Initial Release on Github, Version v1.0.0, Zenodo, doi:10.5281/zenodo.268049
- Albrow, M., Horne, K., Bramich, D. M., et al. 2009, *MNRAS*, 397, 2099
- Batista, V., Beaulieu, J.-P., Bennett, D. P., et al. 2015, *ApJ*, 808, 170
- Bennett, D. P., Anderson, J., & Gaudi, B. S., et al. 2007, *ApJ*, 660, 781
- Bennett, D. P., Batista, V., Bond, I. A., et al. 2014, *ApJ*, 785, 155
- Bennett, D. P., Bhattacharya, A., Anderson, J., et al. 2015, *ApJ*, 808, 169
- Bennett, D. P., Bond, I. A., Udalski, A., et al. 2008, *ApJ*, 684, 663
- Bensby, T., Yee, J. C., Feltzing, S., et al. 2013, *A&A*, 549, 147
- Bessell, M. S., & Brett, J. M. 1988, *PASP*, 100, 1134
- Bond, I. A., Bennett, D. P., Sumi, T., et al. 2017, *MNRAS*, 469, 2434
- Chabrier, G. 2003, *PASP*, 115, 763
- Dong, S., DePoy, D. L., Gaudi, B. S., et al. 2006, *ApJ*, 642, 842
- Gaudi, B. S. 1998, *ApJ*, 506, 533
- Gaudi, B. S. 2012, *ARA&A*, 50, 411
- Gillon, M., Jehin, E., Lederer, S. M., et al. 2016, *Nature*, 533, 221
- Gillon, M., Triaud, A. H. M. J., Demory, B.-O., et al. 2017, *Nature*, 542, 456
- Gould, A., Miralda-Escudé, J., Bahcall, J. N. 1994, *ApJ*, 423, L105
- Gould, A. 2000a, *ApJ*, 535, 928

² Here we exclude systems with $q \gtrsim 0.1$, because the large mass ratios suggest that they are more likely to form via the mechanism similar to that of binary stars rather than that of planetary systems (Lodato et al. 2005).

- Gould, A. 2000b, *ApJ*, 542, 785
- Gould, A., Dong, S., Bennett, D. P., Bond, I. A., Udalski, A., & Kozłowski, S. 2010, *ApJ*, 710, 1800
- Han, C., & Gould, A. 1995, *ApJ*, 447, 53
- Han, C., & Gould, A. 2003, *ApJ*, 592, 172
- Han, C., Jung, Y. K., Udalski, A., et al. 2013, *ApJ*, 778, 38
- Hwang, K.-H., Choi, J.-Y., Bond, I. A., et al. 2013, *ApJ*, 778, 55
- Hwang, K.-H., Ryu, Y.-H., Kim, H.-W., et al. 2019, *AJ*, 157, 23
- Jung, Y. K., Udalski, A., Gould, A., et al. 2018, *AJ*, 155, 219
- Kervella, P., Thévenin, F., Di Folco, E., & Ségransan, D. 2004, *A&A*, 426, 29
- Kim, H.-W., Hwang, K.-H., Shvartzvald, Y., et al. 2018, *AAS* submitted ([arXiv:1806.07545](https://arxiv.org/abs/1806.07545))
- Kim, D.-J., Kim, H.-W., Hwang, K.-H., et al. 2018, *AJ*, 155, 76
- Kim, S.-L., Lee, C.-U., Park, B.-G., et al. 2016, *JKAS*, 49, 37
- Kubas, D., Beaulieu, J. P., Bennett, D. P., et al. 2012, *A&A*, 540, 78
- Laughlin, G., Bodenheimer, P., & Adams, F. C., 2004, *ApJ*, 612, L73
- Lodato, G., Delgado-Donate, E., & Clarke, C. J. 2005, *MNRAS*, 364, L91
- Luhman, K. L. 2012, *ARA&A*, 50, 65
- Nataf, D. M., Gould, A., Fouqué, P., et al. 2013, *ApJ*, 769, 88
- Payne, M. J., & Lodato, G. 2007, *MNRAS*, 381, 1597
- Shvartzvald, Y., Yee, J. C., Calchi Novati, S., et al. 2017, *ApJ*, 840, L3
- Sumi, T., Udalski, A., Bennett, D. P., et al. 2016, *ApJ*, 825, 112
- Szymański, M. K., Udalski, A., Soszyński, I., et al., 2011, *Acta Astron.*, 61, 83
- Tomaney, A. B., & Crots, A. P. S. 1996, *AJ*, 112, 2872
- Udalski, A., Szymański, M. K., & Szymański, G. 2015, *Acta Astron.*, 65, 1
- Vandorou, A., Bennett, D. P., Beaulieu, J.-P., et al. 2020, *AJ*, in press
- Yee, J. C., Han, C., Gould, A., et al. 2014, *ApJ*, 790, 14
- Yee, J. C., Shvartzvald, Y., Gal-Yam, A., et al. 2012, *ApJ*, 755, 102
- Yoo, J., DePoy, D. L., Gal-Yam, A., et al. 2004, *ApJ*, 603, 139
- Zhang, X., Zang, W., Udalski, A., et al. 2019, *AAS* submitted ([arXiv:1911.02439](https://arxiv.org/abs/1911.02439))